AIAA '89

AIAA 89-0643
Artificial Dissipation Sensors for Computational Gasdynamics

G. Dulikravich and D. Dorney, Pennsylvania State Univ., University Park, PA

27th Aerospace Sciences Meeting
January 9–12, 1989/Reno, Nevada

ARTIFICIAL DISSIPATION SENSORS FOR COMPUTATIONAL GASDYNAMICS

George S. Dulikravich and Daniel J. Dorney
Associate Professor Graduate Student
Department of Aerospace Engineering
The Pennsylvania State University
University Park, PA 16802

ABSTRACT

Artificial Dissipation (AD) and Physically Based Dissipation (PBD) models for explicitly added non-physical dissipation in Euler equations of gasdynamics have been compared for the case of a shocked, steady, internal flow. A dissipation sensor function determines the amount of the local dissipation in both formulations. Several new models for the dissipation sensors were introduced and tested. They are based on: second derivative of pressure, gradient of pressure, gradient of Mach number, entropy, vorticity, and divergence of velocity vector. Their ability to generate sharp shocks and their influence on iterative convergence rate were examined indicating the importance of choosing a proper sensor.

INTRODUCTION

Many artificial dissipation models [1-6] used with central difference schemes depend on the use of an artificial dissipation "sensor" to locate regions requiring artificial dissipation. Most dissipation models use an artificial dissipation sensor based on either the second derivative of pressure or the second derivative of density.

While these two types of sensors have been successful in applications, it is not certain if they are the best possible choices. It is the goal of this paper to introduce and test various new artificial dissipation sensors. In particular, we examine artificial dissipation sensors based on: second derivative of pressure, first derivative of pressure, first derivative of Mach number, first derivative of Mach number squared, divergence of the velocity vector, vorticity, and entropy.

The artificial dissipation sensors will be applied to two conceptually different artificial dissipation models. The first dissipation model has been made popular by Jameson et al [1], Chima [2], and others [3,4]. The second dissipation model is the Physically Based Dissipation model proposed by Dulikravich et al [5,6,7].

GOVERNING EQUATIONS

The governing equations considered are the Euler equations of inviscid gasdynamics. The Euler equations in two dimensions and Cartesian coordinates can be expressed in non-dimensional form as:

$$Q_t + E_\xi + F_\eta = 0 \tag{1}$$

where

$$Q = \frac{1}{J}\begin{bmatrix} \rho \\ \rho u \\ \rho v \\ \rho e_o \end{bmatrix} \tag{2}$$

$$E = \frac{1}{J}\begin{bmatrix} \rho U \\ \rho U u + y_\eta p J \\ \rho U v - x_\eta p J \\ \rho U h_o \end{bmatrix} \tag{3}$$

$$F = \frac{1}{J}\begin{bmatrix} \rho V \\ \rho V u - y_\xi p J \\ \rho V v + x_\xi p J \\ \rho V h_o \end{bmatrix} \tag{4}$$

Here, ρ is the density, u is the x-component of velocity, v is the y-component of velocity, p is the thermodynamic pressure, e_o is the total mass-specific energy and h_o is the total mass-specific enthalpy.

The total mass-specific energy can be written as:

$$e_o = \frac{p}{\rho(\gamma-1)} + \frac{1}{2}(u^2+v^2) \tag{5}$$

and the total mass-specific enthalpy can be expressed as:

$$h_o = e_o + p/\rho \tag{6}$$

The curvilinear nonorthogonal coordinates following the grid lines are

$$\xi = \xi(x,y) \quad y = \eta(x,y) \tag{7}$$

so that the contravariant velocity vector components are

$$U = (uy_\eta - vx_\eta)J \; ; \; V = (vx_\xi - uy_\xi)J \text{ where} \tag{8}$$

$$y_\eta = \xi_x/J; \; y_\xi = -\eta_x/J; x_\eta = -\xi_y/J; \; x_\xi = \eta_y/J \tag{9}$$

Here, the Jacobian of the geometric transformation is

$$J = \det^{-1} \frac{\partial(x,y)}{\partial(\xi,\eta)} = (x_\xi y_\eta - y_\xi x_\eta)^{-1} \quad (10)$$

ARTIFICIAL DISSIPATION MODELS

Two dissipation models will be used to investigate the influence of different artificial dissipation sensors. The first dissipation model has been made popular by Jameson et al [1] and will be referred to as Jameson's dissipation model. The second dissipation model is the recently developed Physically Based Dissipation model [5,6,7].

In Jameson's dissipation, the equations of motion (1) are first rewritten to include the dissipation terms:

$$Q_t + E_\xi + F_\eta = D(Q) \quad (11)$$

where D is an explicitly added dissipative operator.

In Jameson's dissipation model, the construction of the dissipative terms for each of the four equations is similar. For example, the continuity equation artificial dissipation is

$$D\rho = D_\xi\rho + D_\eta\rho \quad (12)$$

where

$$D_\xi\rho = d_{i+1/2,j} - d_{i-1/2,j} \quad (13)$$

$$D_\eta\rho = d_{i,j+1/2} - d_{i,j-1/2} \quad (14)$$

The terms on the right hand side of the equations in the system (1) all have the similar form [1]. For example,

$$d_{i+1/2,j} = \frac{J_{i+1/2,j}}{\Delta t} \{\epsilon^{(2)}_{i+1/2,j} (\rho_{i+1,j} - \rho_{i,j}) + \epsilon^{(4)}_{i+1/2,j}(\rho_{i+2,j} - 3\rho_{i+1,j} + 3\rho_{i,j} - \rho_{i-1,j})\} \quad (15)$$

where $\epsilon^{(2)}$ and $\epsilon^{(4)}$ are flow adaptive coefficients:

$$\epsilon^{(2)}_{i+1/2,j} = k^{(2)} \max(\upsilon_{i+1,j}, \upsilon_{i,j}) \quad (16)$$

and

$$\epsilon^{(4)}_{i+1/2,j} = \max(0., (\kappa^{(4)} - \epsilon^{(2)}_{i+1/2,j})) \quad (17)$$

Here, υ represents an artificial dissipation sensor.

Here, $\kappa^{(2)}$ and $\kappa^{(4)}$ are user-specified coefficients. The suggested values are

$$\kappa^{(2)} = \frac{1}{4} \quad \text{and} \quad \kappa^{(4)} = \frac{1}{256} \quad (18)$$

although considerably different values need to be used in practice thus requiring a considerable level of experience on the part of a user.

The second dissipation model is the recently developed Physically Based Dissipation (PBD) model [5,6,7]. In this model, the dissipation is based on actual physical dissipation. To solve the Euler equations, here one actually solves the Navier-Stokes equations of viscous and heat conducting flow subject to perfect slip boundary conditions and spatially varying coefficients of viscosity. Thus, the PBD model represents a physically consistent formulation since the Euler equations of inviscid gasdynamics represent a limiting case of the Navier-Stokes equations as the physical dissipation becomes negligible.

The Navier-Stokes equations of unsteady, viscous, laminar flow allowing for heat conduction assuming Fourier's law can be expressed in non-dimensional form and transformed coordinates as:

$$Q_t + E_\xi + F_\eta = \frac{1}{R_e}(E^v_\xi + F^v_\eta) \quad (19)$$

where R_e is the Reynolds number. The generalized viscous flux vectors are:

$$E^v = \frac{1}{J}\begin{bmatrix} 0 \\ E_1 \\ E_2 \\ E_3 \end{bmatrix} \quad (20)$$

$$F^v = \frac{1}{J}\begin{bmatrix} 0 \\ F_1 \\ F_2 \\ F_3 \end{bmatrix} \quad (21)$$

where

$$\begin{bmatrix} E_1 & E_2 \\ F_1 & F_2 \end{bmatrix} = \begin{bmatrix} \xi_x & \xi_y \\ \eta_x & \eta_y \end{bmatrix} \begin{bmatrix} \tau_{xx} & \tau_{xy} \\ \tau_{yx} & \tau_{yy} \end{bmatrix} \quad (22)$$

and

$$\begin{bmatrix} E_3 \\ F_3 \end{bmatrix} = \begin{bmatrix} \xi_x & \xi_y \\ \eta_x & \eta_y \end{bmatrix} \begin{bmatrix} \tau_{xx} & \tau_{xy} \\ \tau_{yx} & \tau_{yy} \end{bmatrix} \begin{bmatrix} u \\ v \end{bmatrix} - \begin{bmatrix} \xi_x & \xi_y \\ \eta_x & \eta_y \end{bmatrix} \begin{bmatrix} q_x \\ q_y \end{bmatrix} \quad (23)$$

The components of the non-dimensional viscous stress tensor

expressed in terms of ξ,η coordinates are:

$$\tau_{xx} = [\mu'' (u_\xi y_\eta - u_\eta y_\xi) + \lambda (v_\eta x_\xi - v_\xi x_\eta)]J \quad (24)$$

$$\tau_{yy} = [\mu'' (v_\eta x_\xi - v_\xi x_\eta) + \lambda (u_\xi y_\eta - u_\eta y_\xi]J \quad (25)$$

$$\tau_{xy} = \mu (u_\eta x_\xi - u_\xi x_\eta + v_\xi y_\eta - v_\eta y_\xi)J \quad (26)$$

and the non-dimensional heat conduction fluxes are

$$q_x = \frac{\mu}{(\gamma-1)M_\infty^2 P_r}(T_\xi y_\eta - T_\eta y_\xi)J \quad (27)$$

$$q_y = \frac{\mu}{(\gamma-1)M_\infty^2 P_r}(T_\eta x_\xi - T_\xi x_\eta)J \quad (28)$$

Here, $\mu'' = 2\mu + \lambda$ is the longitudinal viscosity coefficient, μ is the shear viscosity, λ is the secondary viscosity, M_∞ is the freestream Mach number, P_r is the Prandtl number and T is the absolute temperature. In the PBD formulation, the shear viscosity coefficient, μ, is forced to vary throughout the flowfield by means of an appropriate artificial dissipation sensor, ν, similar to one used in equation 16. For example, when using the PBD formulation for Euler equations, one should actually program complete Navier-Stokes equations and use $\mu=\mu\nu$ and Stokes hypothesis ($\lambda/\mu = -2/3$). When using the PBD concept with Navier-Stokes equations, the modified coefficient of viscosity could be: $\mu = \mu(1+\nu)$.

ARTIFICIAL DISSIPATION SENSORS

Since a finite volume scheme is used, flow variables are defined at cell centers. Different values for the artificial dissipation sensor are obtained for the ξ and η directions. The resulting values for the dissipation sensor are obtained at cell boundaries.

The first sensor to be discussed is the one commonly used with the existing dissipation models. It is based on the second derivative of pressure (P2 sensor). For example, in the ξ direction, this sensor can be written as [1,2]:

$$\nu_{i,j} = C\frac{|p_{i+1,j} - 2p_{i,j} + p_{i-1,j}|}{p_{i+1,j} + 2p_{i,j} + p_{i-1,j}} \quad (29)$$

where C is the user specified constant. The numerator of equation (29) is the second derivative of pressure, while the denominator scales the terms with the local values of the pressure. This sensor has been relatively successful in engineering applications although it experiences obvious difficulties in the vicinity of stagnation points. An attempt to alleviate this problem was to premultiply the sensor with the local value of the Mach number [3].

Instead of the second derivative of pressure, one could use an artificial dissipation sensor based on the first derivative of pressure (P1 sensor) which is explicitly found in the Navier-Stokes equations. The sensor is implemented as:

$$\nu_{i+1/2,j} = C\frac{|p_{i+1,j} - p_{i,j}|}{p_{i+1,j} + p_{i,j}} \quad (30)$$

A similar sensor can be introduced that is based on the first derivative of the Mach number (M1 sensor).

$$\nu_{i+1/2,j} = C|M_{i+1,j} - M_{i,j}| \quad (31)$$

The artificial dissipation sensor can be based on the divergence of the velocity vector (DIV sensor).

The value of the divergence of the velocity vector can be viewed as the deviation from incompressibility and will have large values at the shock wave. Written in transformed (ξ,η) coordinates, this sensor is:

$$\nu_{i+1/2,j} = C|u_\xi y_\eta - u_\eta y_\xi + v_\eta x_\xi - v_\xi x_\eta|_{i+1/2,j} J_{i+1/2,j} \quad (32)$$

Since vorticity is generated at the curved shock surface in an otherwise irrotational flow, the artificial dissipation sensor can be based on the curl of the velocity vector, i.e., the vorticity (VOR sensor)

$$\nabla \times \vec{V} = v_x - u_y \quad (33)$$

For irrotational flow, equation (33) equals zero. Written in transformed coordinates, the vorticity sensor is:

$$\nu_{i+1/2,j} = C|v_\xi y_\eta - v_\eta y_\xi - u_\eta x_\xi + u_\xi x_\eta|_{i+1/2,j} J_{i+1/2,j} \quad (34)$$

The last sensor investigated is based on the change of the entropy

$$S = S_\infty + C_v \ln[(\frac{p}{p_\infty})(\frac{\rho_\infty}{\rho})^\gamma] \quad (35)$$

where S is the entropy and C_v is the specific heat at constant volume. Then

$$\nu_{i+1/2,j} = C\left|\left(S_\infty + C_v \ln\left[\left(\frac{p_{i+1,j}}{p_\infty}\right)\left(\frac{\rho_\infty}{\rho_{i+1,j}}\right)^\gamma\right]\right)\right.$$

$$\left. - \left(S_\infty + C_v \ln\left[\left(\frac{p_{i,j}}{p_\infty}\right)\left(\frac{\rho_\infty}{\rho_{i,j}}\right)^\gamma\right]\right)\right| \qquad (36)$$

Hence, the entropy based sensor (ENT sensor) can be

$$\nu_{i+1/2,j} = C\left|C_v \ln\left[\left(\frac{p_{i+1,j}}{p_{i,j}}\right)\left(\frac{\rho_{i,j}}{\rho_{i+1,j}}\right)^\gamma\right]\right| \qquad (37)$$

EQUIVALENT LOCAL REYNOLDS NUMBER

Then, the thickness, δx, of the weak shock wave can be obtained from the relation [8]

$$\frac{\bar{\rho}_1 \bar{a}_1 \delta\bar{x}}{\bar{\mu}} = \frac{4M_1}{M_1^2-1}\left(\frac{4}{3} + \frac{\gamma-1}{\gamma}\,\frac{9\gamma-5}{4}\right) \qquad (38)$$

where $\bar{a}$ is the speed of sound and the subscript (1) designates location immediately upstream of the shock wave and the overbars designate dimensional quantities.

It follows that

$$\frac{\bar{\mu}}{\bar{\rho}_e \bar{a}_e \bar{L}_e} \geq \left(\frac{M_{e1}^2 - \left(\frac{\gamma+1}{2} - \frac{\gamma-1}{2}M_{e1}^2\right)}{M_{e1}}\right)\left(\frac{\gamma+1}{2} - \frac{\gamma-1}{2}M_{e1}^2\right)^{\frac{1}{\gamma-1}}$$

$$\frac{(\gamma+1)}{2}\;\frac{\delta x}{\frac{(9\gamma-5)(\gamma-1)}{\gamma} + \frac{16}{3}} \qquad (39)$$

If one knows that a particular numerical algorithm needs a minimum of N grid cells, that is $N\Delta x$, to resolve a shock wave, then δx in the above expression can be replaced with $N\Delta x$ in order to determine the "equivalent" value of the non-physical local Reynolds number, $(R_e)_{EQ}$. Thus, the equivalent nondimensional shear viscosity is

$$\left(\frac{1}{Re}\right)_{EQ} \geq \frac{\left[M_{e1}^2 - \left(\frac{\gamma+1}{2} - \frac{\gamma-1}{2}M_{e1}^2\right)\right]}{M_{e1}}\left(\frac{\gamma+1}{2} - \frac{\gamma-1}{2}M_{e1}^2\right)^{\frac{1}{\gamma-1}}$$

$$\cdot\left(\frac{\gamma+1}{2}\right) N\Delta x \,/\left[\frac{(9\gamma-5)(\gamma-1)}{\gamma} + \frac{16}{3}\right] \qquad (40)$$

For example, if $\gamma = 7/5$, $N = 3$, $\Delta x = 3/80$, then the above equation gives the following upper limits for $(R_e)_{EQ}$.

M_1	1.1	1.2	1.3	1.4	1.5	1.6	1.7
$(R_e)_{EQ}$	322.8	187.5	145.2	126.5	117.7	114.1	113.7

Using a heuristic analysis, one can determine approximately the minimum allowable Reynolds number. The definition of the local time step considering CFL and diffusion limitations is given for the x direction by [9]

$$\Delta t \leq \min\left(\frac{\Delta x}{|u|+c + \alpha\bar{\mu}/\Delta x}\right) \qquad (41)$$

where α is a constant and $\bar{\mu}$ combines the effects of physical and artificial viscosity [10]

$$\bar{\mu} = \mu_{phy} + \mu_{art} \qquad (42)$$

For the Euler equations $\mu_{phy} = 0$.
Then, if the time step is known from the inviscid analysis:

$$\mu_{art} \leq \left[\frac{\Delta x}{\Delta t} - |u| - c\right]\frac{\Delta x}{\alpha} \qquad (43)$$

Introducing the definition of the equivalent Reynold's number:

$$\left(\frac{1}{R_e}\right)_{EQ} \leq \left(\frac{1}{\rho u L}\right)\frac{\Delta x}{\alpha}\left[\frac{\Delta x}{\Delta t} - |u| - c\right] \qquad (44)$$

RESULTS

The basic computer code used in this investigation was developed following the original work of Jameson [1] with an option to use his Artificial Dissipation (AD) or the Physically Based Dissipation (PBD). Nevertheless, the AD formulation was run without the fourth order dissipative term. The results obtained with PBD formulation used Re=100. Geometry consisted of a straight channel with a 10% thick half-airfoil attached to the upper wall. Leading and trailing edge points of the airfoil were smoothed. Computational grid (Fig. 1) consisted of 64 x 16 grid cells. All runs were preformed for 1500 iterations on Vax 8600 with uniform flow at $M_\infty = 0.675$ as an initial guess.

Fig. 2 depicts the oscillations which develop away from the shock when AD is used with P2 sensor, but without the fourth order dissipation. For

comparison, PBD with the entropy sensor (ENT) and low value of the constant (C=0.013) gives a smoother solution. From the following results it could be concluded that AD formulation without the fourth order dissipation is quite feasible if the P2 sensor is replaced by some other type of a sensor.

Fig. 3 and Fig. 4 compare Mach number distributions on the lower and upper walls obtained when using second derivative of pressure (P2) as a sensor in AD and in PBD formulation. The AD formulation seems to capture peak Mach number better although the conclusion is reversed when using pressure gradient (P1) sensor (Fig. 5 and Fig. 6). When using Mach number gradient (M1) sensor, both AD and PBD formulation underestimate the peak value of the Mach number and smear the shock (Fig. 7 and Fig. 8). The entropy sensor (ENT) with a low value of the constant seems to offer an exceptionally sharp shock and the post-shock recovery (Fig. 9) when used with AD formulation. The same sensor used with the PBD formulation produced somewhat smoother (Fig. 10) solutions. The vorticity sensor (VOR) gives considerably better results with PBD than with the AD formulation (Fig. 11 and Fig. 12). Similar conclusion is evident when using divergence of the velocity vector (DIV) sensor (Fig. 13 and Fig. 14).

Summaries of results obtained with different artificial dissipation sensors applied to AD and to PBD formulations are given in Fig. 15 and Fig. 16. In general, it seems that the low value of ENT sensor and the DIV sensor offer the best results with both AD and PBD. The lowest curve showing an entirely smeared solution in Fig. 15 was obtained when using large value for the constant (C=0.1) with ENT sensor. The summary of values for the constant C used in this investigation is given below:

	P2	P1	M1	ENT	VOR	DIV
AD	0.7	0.7	1.0	0.013	0.02	0.02
PBD	30.0	15.0	30.0	0.6	0.6	0.3

Notice that these values are by no means optimal and that M1, ENT, VOR and DIV sensors have not been normalized in our formulations. Also, AD formulation scales the dissipation term with the local value of the Jacobian, while PBD formulation did not use this feature.

Convergence histories of the AD and the PBD formulation with different dissipation sensors (Fig. 17 and Fig. 18) indicate that significantly different convergence rates are attainable with different sensors. ENT and M1 sensors weem to offer the fastest convergence rates, while VOR and P2 sensors offer the slowest convergence. The peculiar spikes in the convergence histories obtained with VOR and DIV sensors are due to the logic used in the codes that the local value of such a sensor should be the maximum of the three neighboring cells instead of the average of the neighboring cells.

Isobars for the flowfield are depicted for both AD and PBD formulation when using P2 sensor (Fig. 19 and Fig. 20), P1 sensor (Fig. 21 and Fig. 22), M1 sensor (Fig. 23 and Fig. 24), ENT sensor with low value for C (Fig. 25 and Fig. 26), VOR sensor (Fig. 27 and Fig. 28), and DIV sensor (Fig. 20 and Fig. 30). Again, ENT sensor obviously gives the sharpest shock.

CONCLUSIONS

Preliminary numerical results indicate that the form of artificial dissipation sensor can significantly affect the numerical solution and the iterative convergence rate. The Mach number and entropy sensors have been found to greatly enhance the convergence. The velocity divergence and vorticity sensors appear to offer better shock resolution than the other sensors, with the exception of low entropy sensor which generates a sharp shock and post-shock recovery region. All the sensors investigated yield stable solutions.

ACKNOWLEDGEMENTS

The authors would like to express their thanks to Ms. Amy Myers for her expert typing and to Apple Computer, Inc. for the computing equipment.

REFERENCES

1. Jameson, A., Schmidt, W., and Turkel, E., "Numerical Solutions of the Euler Equations by Finite Volume Methods Using Runge-Kutta Time-Stepping Schemes," AIAA Paper 81-1259, 14th Fluid and Plasma Dynamics Conference, Palo Alto, CA, June 23-25, 1981.

2. Chima, R. V., "Analysis of Inviscid and Viscous Flows in Cascades with an Explicit Multiple-Grid Algorithm," AIAA J., Vol. 23, No. 10, Oct. 1985, pp. 1556-1563.

3. Caughey, D. A. and Turkel, E., "Effects of Numerical Dissipation on Finite-Volume Solutions of Compressible Flow Problems," AIAA Paper 88-0621, 26th Aerospace Sciences Meeting, Reno, NV, January 11-14, 1988.

4. Chima, R. V., Turkel, E. and Schaffer, S., "Comparison of Three Explicit Multigrid Methods for the Euler and Navier-Stokes Equations," AIAA Paper 87-0602, 25th Aerospace Sciences Meeting, Reno, NV, January 12-15, 1987.

5. Dulikravich, G. S., Dorney, D. J. and Lee, S., "Iterative Acceleration and Physically Based Dissipation for the Euler Equations of Gasdynamics," presented at the ASME Winter Annual Meeting, Nov. 28 - Dec. 2, 1988.

6. Dulikravich, G. S., Dorney, D. J. and Lee, S., "Numerical Versus Physical Dissipation in the Solution of Compressible Navier-Stokes Equations," AIAA paper 89-0550, 27th Aerospace Sciences Meeting, Reno, NV, Jan. 9-12, 1989.

7. Dorney, D. J., Dulikravich, G. S. and Lee, K., "A Comparative Study of Iterative Algorithms for the Euler Equations of Gasdynamics," AIAA paper 89-0114, 27th Aerospace Sciences Meeting, Reno, NV, January 8-12, 1989.

8. Patterson, G. N., "Transition Through Weak Shock Front," Univ. of Toronto, UTIA Report No. 1, May 1948.

9. Richtmyer, R. D. and Morton, K. W., Difference Methods for Initial Value Problems, Wiley, New York, 1967.

10. Davis, R. L., Ni, R. H. and Carter, J. E., "Cascade Viscous Flow Analysis Using Navier-Stokes Equations," AIAA Paper 86-0033.

11. Tong, S. S., "The Impact of Smoothing Formulations on the Stability and Accuracy of Various Time Marching Schemes," AIAA Paper 87-1106.

12. Merriam, M., "Smoothing and the Second Law," First World Congress on Computational Mechanics, Austin, TX, September 22-26, 1986.

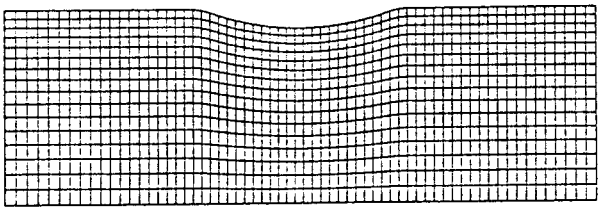

Fig.1 Computational grid for a 10% half-airfoil in a channel

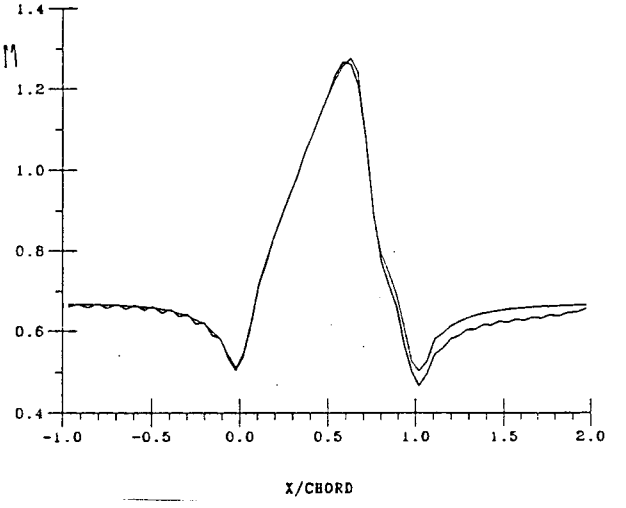

Fig.2 Upper wall Mach number values: PBD with low entropy sensor and AD without fourth order dissipation

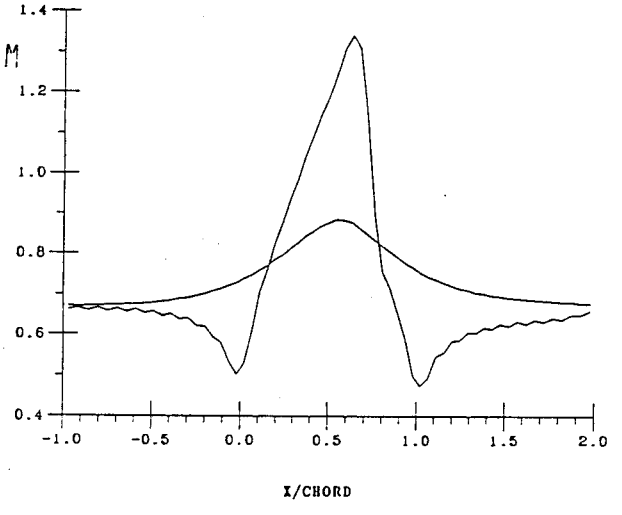

Fig.3 AD with P2 sensor: Mach number distributions on channel walls.

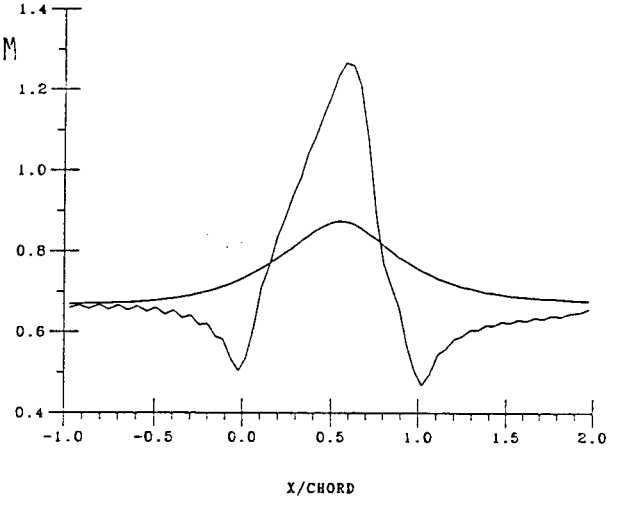

Fig.4 PBD with P2 sensor: Mach number distributions on channel walls.

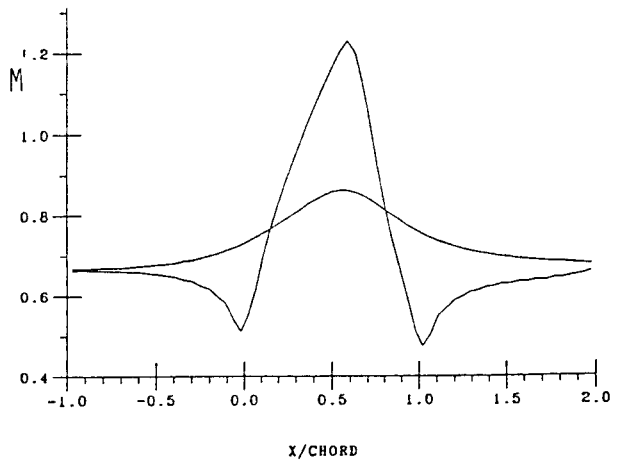

Fig.5 AD with P1 sensor: Mach number distributions on channel walls.

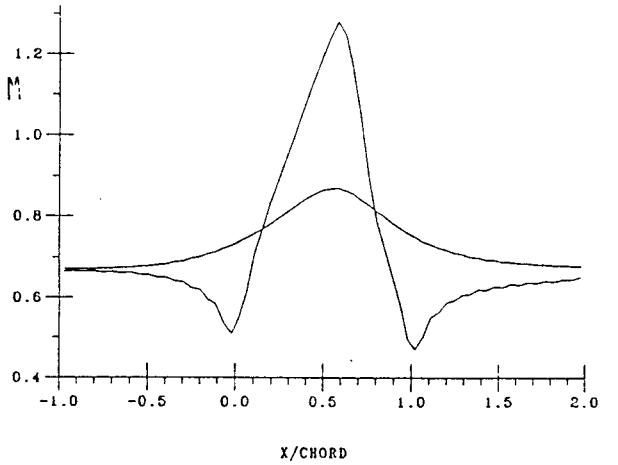

Fig.6 PBD with P1 sensor: Mach number distributions on channel walls.

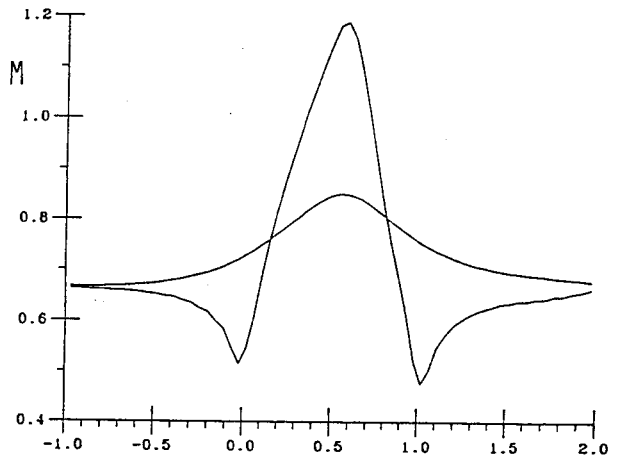

Fig.7 AD with M1 sensor: Mach number distributions on channel walls.

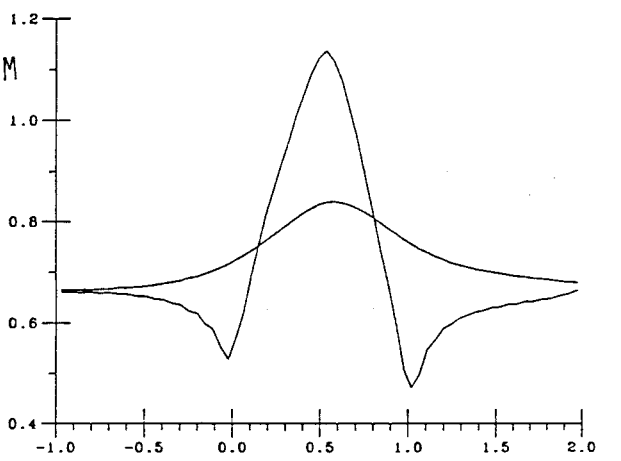

Fig.8 PBD with M1 sensor: Mach number distributions on channel walls.

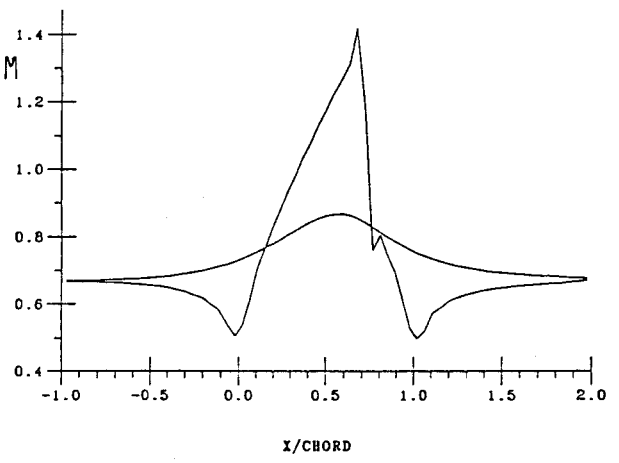

Fig.9 AD with ENT sensor: Mach number distributions on channel walls.

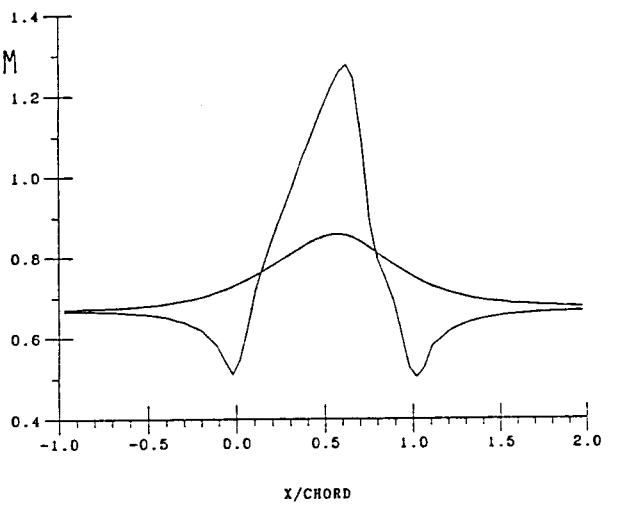

Fig.10 PBD with ENT sensor: Mach number distributions on channel walls.

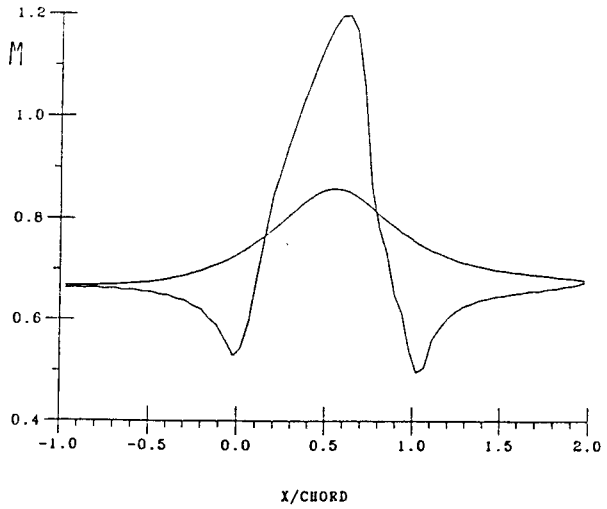

Fig.11 AD with VOR sensor: Mach number distributions on channel walls.

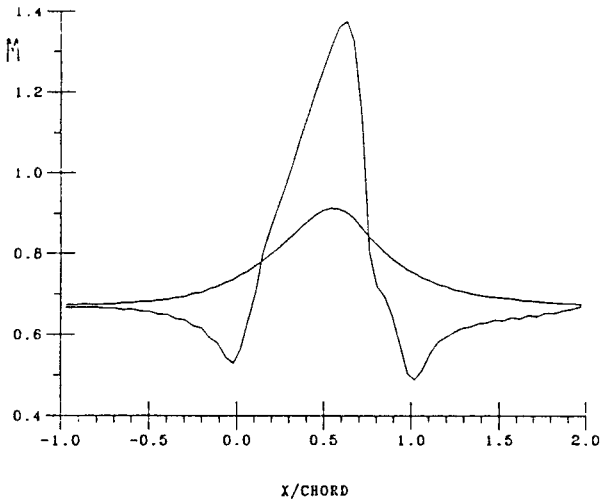

Fig.12 PBD with VOR sensor: Mach number distributions on channel walls.

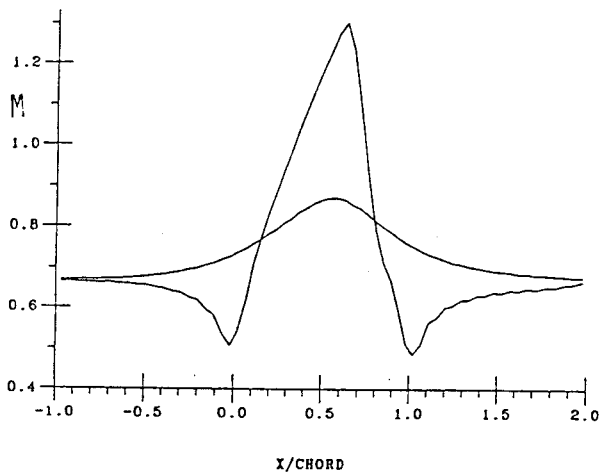

Fig.13 AD with DIV sensor: Mach number distributions on channel walls.

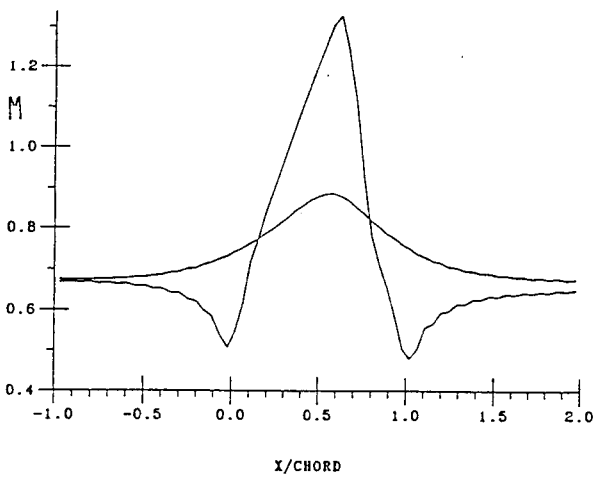

Fig.14 PBD with DIV sensor: Mach number distributions on channel walls.

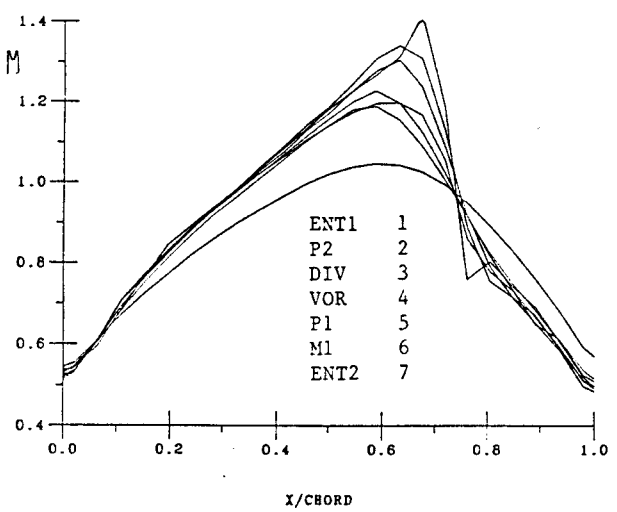

Fig.15 AD with different sensors: Mach number distributions on upper wall.

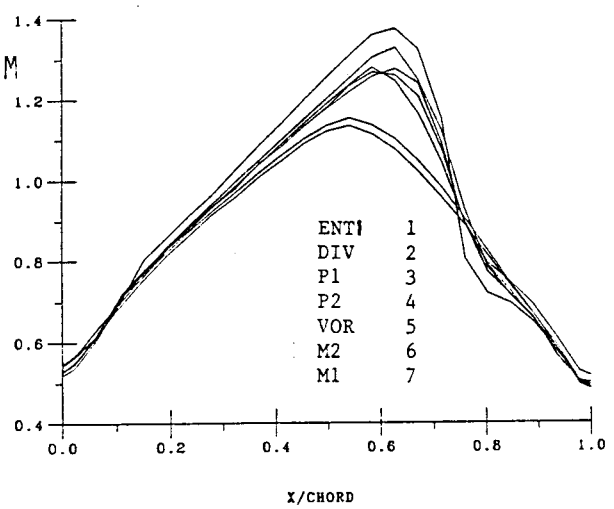

Fig.16 PBD with different sensors: Mach number distributions on upper wall.

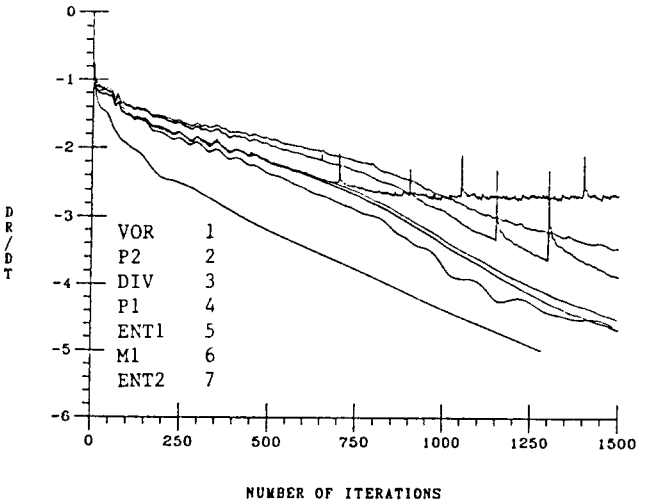

Fig.17 AD convergence histories with different sensors.

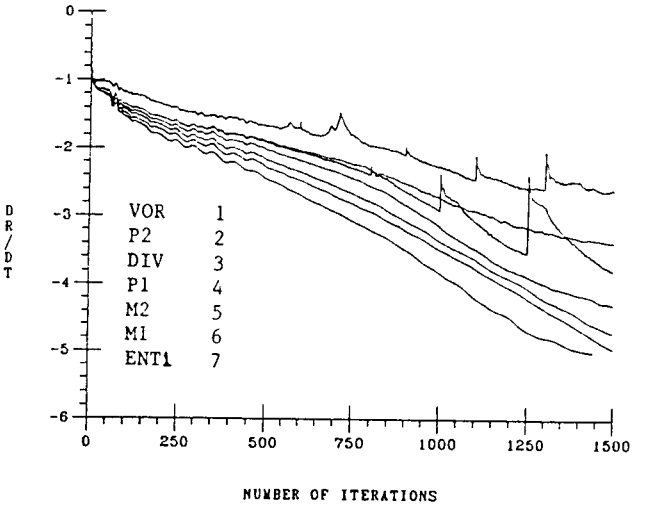

Fig.18 PBD convergence histories with different sensors.

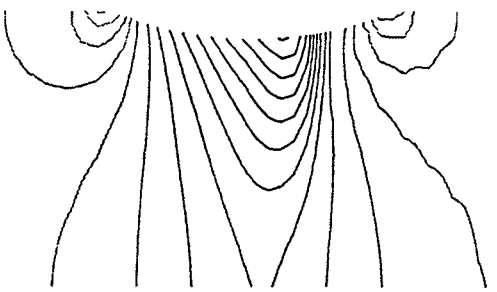

Fig.19 AD with P2 sensor: isobars

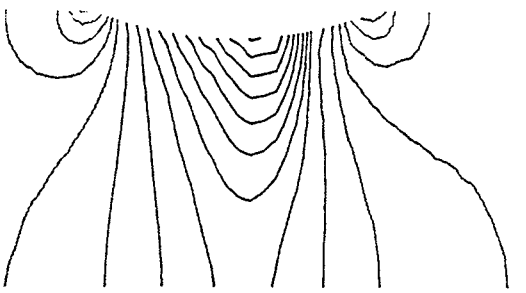

Fig.20 PBD with P2 sensor: isobars

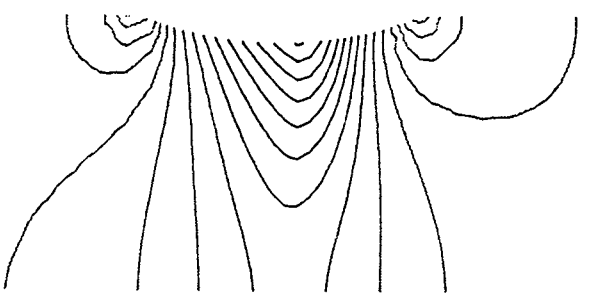

Fig.21 AD with P1 sensor: isobars

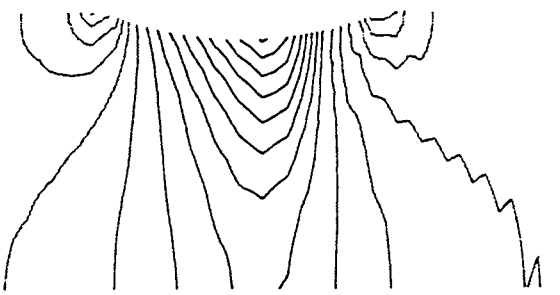

Fig.22 PBD with P1 sensor: isobars

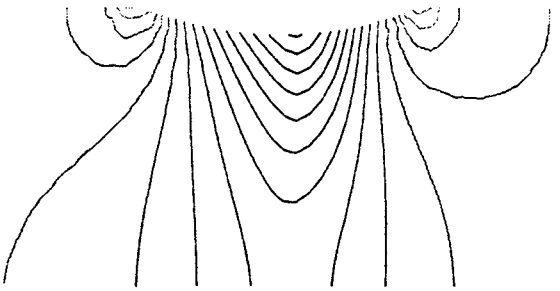

Fig.23 AD with M1 sensor: isobars

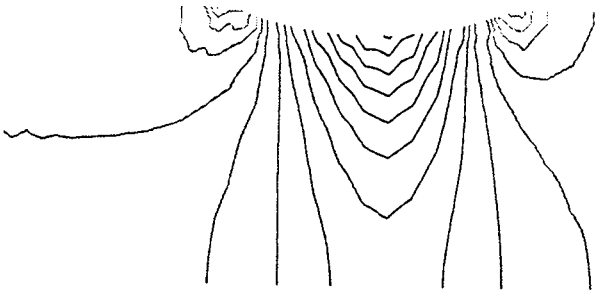

Fig.24 PBD with M1 sensor: isobars

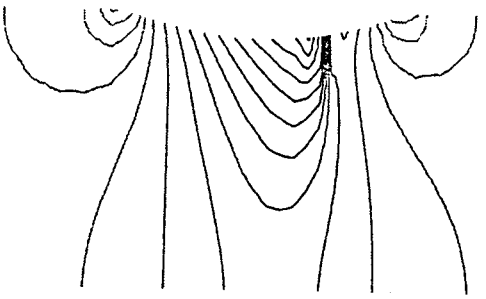

Fig.25 AD with ENT sensor: isobars

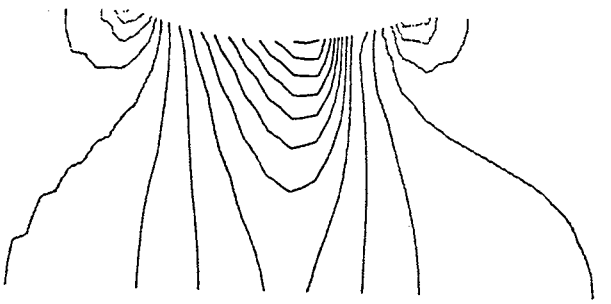

Fig.26 PBD with ENT sensor: isobars

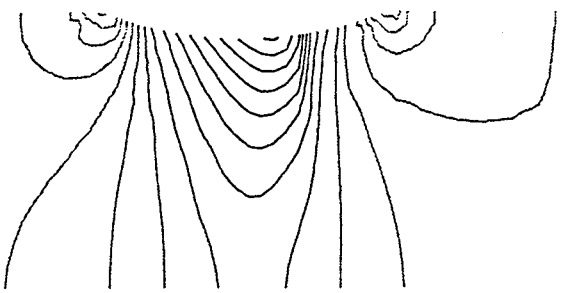

Fig.27 AD with VOR sensor: isobars

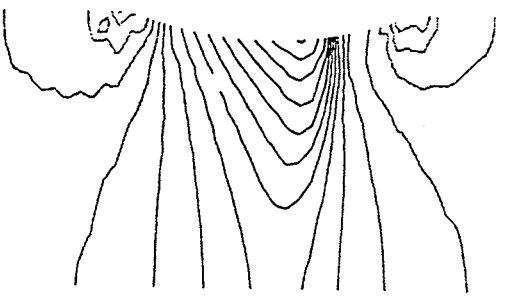

Fig.28 PBD with VOR sensor: isobars

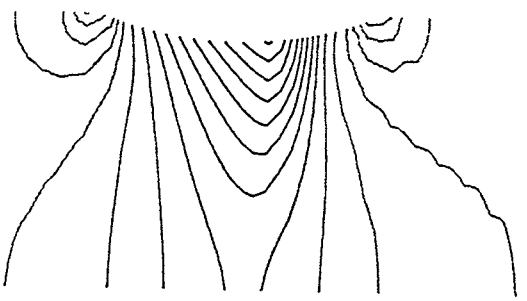

Fig.29 AD with DIV sensor: isobars

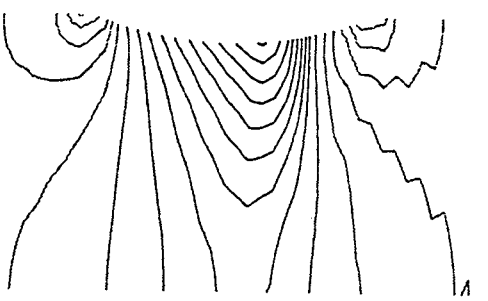

Fig.30 PBD with DIV sensor: isobars